

Mg II and Fe II fluxes of luminous quasars at $z \sim 2.7$ and evaluation of the Baldwin effect in the flux-to-abundance conversion method for quasars

HIROAKI SAMESHIMA ¹, YUZURU YOSHII,^{1,2} NORIYUKI MATSUNAGA,^{3,4} NAOTO KOBAYASHI,^{5,1,4} YUJI IKEDA ^{4,6},
SOHEI KONDO,^{5,4} SATOSHI HAMANO ^{7,4}, MISAKI MIZUMOTO,^{8,9} AKIRA ARAI,⁴ CHIKAKO YASUI,^{10,4} KEI FUKUE,⁴
HIDEYO KAWAKITA ^{4,11}, SHOGO OTSUBO,⁴ GIUSEPPE BONO,^{12,13} AND IVO SAVIANE ¹⁴

¹*Institute of Astronomy, School of Science, The University of Tokyo, 2-21-1 Osawa, Mitaka, Tokyo 181-0015, Japan*

²*Steward Observatory, University of Arizona, 933 North Cherry Avenue, Room N204, Tucson, AZ 85721-0065, USA*

³*Department of Astronomy, Graduate School of Science, The University of Tokyo, 7-3-1 Hongo, Bunkyo-ku, Tokyo 113-0033, Japan*

⁴*Laboratory of Infrared High-resolution spectroscopy (LiH), Koyama Astronomical Observatory, Kyoto Sangyo University, Motoyama, Kamigamo, Kita-ku, Kyoto 603-8555, Japan*

⁵*Kiso Observatory, Institute of Astronomy, School of Science, The University of Tokyo, 10762-30 Mitake, Kiso-machi, Kiso-gun, Nagano, 397-0101, Japan*

⁶*Photocoding, 460-102 Iwakura-Nakamachi, Sakyo-ku, Kyoto, 606-0025, Japan*

⁷*National Astronomical Observatory of Japan, 2-21-1 Osawa, Mitaka, Tokyo 181-8588, Japan*

⁸*Hakubi Center, Kyoto University, Yoshida-honmachi, Sakyo-ku, Kyoto 606-8501, Japan*

⁹*Department of Astronomy, Graduate School of Science, Kyoto University, Kitashirakawa-otwakecho, Sakyo-ku, Kyoto 606-8502, Japan*

¹⁰*National Astronomical Observatory of Japan, California office, 100 W. Walnut St., Suite 300, Pasadena, CA 91124, USA*

¹¹*Department of Astrophysics and Atmospheric Sciences, Faculty of Sciences, Kyoto Sangyo University, Motoyama, Kamigamo, Kita-ku, Kyoto 603-8555, Japan*

¹²*Dipartimento di Fisica, Università di Roma Tor Vergata, via della Ricerca Scientifica 1, I-00133 Roma, Italy*

¹³*INAF-Osservatorio Astronomico di Roma, via Frascati 33, I-00078 Monte Porzio Catone, Italy*

¹⁴*European Southern Observatory, Alonso de Cordova 3107, Santiago, Chile*

ABSTRACT

To investigate the chemical abundance of broad-line region clouds in quasars at high redshifts, we performed near-infrared spectroscopy of six luminous quasars at $z \sim 2.7$ with the WINERED spectrograph mounted on the New Technology Telescope (NTT) at the La Silla Observatory, Chile. The measured Fe II/Mg II flux ratios nearly matched with the published data for $0.7 \lesssim z \lesssim 1.6$, suggesting that there is no evolution over a long period of cosmic time, which is consistent with previous studies. To derive the chemical abundances from the measured equivalent widths (EWs), their dependence on nonabundance factors must be corrected. In our previous paper, we proposed a method to derive the [Mg/Fe] abundance ratio and the [Fe/H] abundance by correcting the dependence of EW(Mg II) and EW(Fe II) on the Eddington ratio. To the best of our knowledge, that was the first report to discuss the star-formation history through a direct comparison with chemical evolution models. In the present study, we further investigated the dependence of EWs on luminosity, which is known as the Baldwin effect (BEff). Additional correction for the BEff significantly affects the derived chemical abundances for the six luminous quasars at $z \sim 2.7$, and the resultant abundances agree well with the prediction of chemical evolution models. Given that most distant quasars found thus far are biased toward luminous ones, the correction of the measured EWs for the BEff is crucial for extending the chemical evolution study to higher redshifts.

Keywords: galaxies: abundances — galaxies: active — quasars: emission lines — galaxies: evolution — cosmology: observations — early universe

1. INTRODUCTION

Many researchers have investigated the chemical evolution of the universe using distant quasars at high redshifts. This is mostly because the associated history of

formation and evolution of massive stars is expected to drive the chemical evolution, as well as circulate gaseous material and provide thermal and kinetic energy to the early universe (e.g., Vogelsberger et al. 2014; Schaye et al. 2015; Pillepich et al. 2018).

Heavy elements in the broad-line region (BLR) clouds of quasars are produced by the supernova explosion of stars that are formed in host galaxies (Hamann & Ferland 1999). α elements such as Mg are ejected from Type II supernovae (SNe II), which are formed when short-lived massive stars die. In contrast, a considerable amount of Fe originates from Type Ia supernovae (SNe Ia), which are formed when long-lived intermediate-mass stars in a binary system explode. Thus, Fe enrichment is significantly delayed compared with α elements. This causes a break in the $[\alpha/\text{Fe}]$ ¹ ratio at the cosmic time elapsed since the formation of the first stars, $t - t_0$, which corresponds to the typical lifetime t_{Ia} of an SN Ia progenitor. This $[\alpha/\text{Fe}]$ break as a nucleosynthetic conjecture (Tinsley 1979) has been confirmed by observations of metal-poor stars in the Galactic thin and thick disks (e.g., McWilliam 1997; Feltzing et al. 2003) and in dwarf spheroidal galaxies (e.g., Tolstoy et al. 2009). However, a clear signature of the $[\alpha/\text{Fe}]$ break has not been observed yet in distant quasars, and it is being actively explored for high redshifts (e.g., De Rosa et al. 2014; Mazzucchelli et al. 2017; Onoue et al. 2020).

Thus far, measuring the emission-line flux ratio has been considered a promising method for deriving $[\alpha/\text{Fe}]$; the ultraviolet (UV) emission lines of Mg II $\lambda 2798$ and Fe II, which exhibits a broad composite feature at $\sim 2000\text{--}3000 \text{ \AA}$, have been considered as an ideal line pair (e.g., Wills et al. 1985). Thus the Fe II/Mg II flux ratio of quasars has been measured over a wide range of redshift extending to $z \sim 7$ by many researchers (e.g., Kawara et al. 1996; Thompson et al. 1999; Freudling et al. 2003; Barth et al. 2003; Maiolino et al. 2003; Dietrich et al. 2002a, 2003; Iwamuro et al. 2002, 2004; Tsuzuki et al. 2006; Jiang et al. 2007; Kurk et al. 2007; Sameshima et al. 2009; De Rosa et al. 2011, 2014; Mazzucchelli et al. 2017; Shin et al. 2019; Onoue et al. 2020). However, the measured flux ratios deviate significantly beyond the measurement error range,² preventing us from finding any signature of the $[\text{Mg}/\text{Fe}]$ evolution over

a range of redshift explored. Hence, it was uncertain whether the assumption that the Fe II/Mg II flux ratio was a first-order proxy for $[\text{Mg}/\text{Fe}]$ was correct (e.g., Dong et al. 2011; De Rosa et al. 2011).

As a turning point in this research area, we developed a method for abundance diagnostics of BLR clouds (Sameshima et al. 2017; hereafter, Paper I), which compares the measured equivalent widths (EWs) of Mg II and Fe II that are corrected for their dependence on the Eddington ratio with detailed photoionization simulations. It was shown, for the first time, that the derived $[\text{Mg}/\text{Fe}]$ abundance ratio and $[\text{Fe}/\text{H}]$ abundance agreed well with the prediction of chemical evolution models for the redshift range of $0.7 \lesssim z \lesssim 1.6$. However, because the chemical evolution models converge at $z \lesssim 2$ regardless of the star-formation history in the early universe, the most plausible model has not been determined yet.

Thus, high-redshift data are vital to overcome the indistinguishability at $z \lesssim 2$ in chemical evolution models. High-redshift quasars that have been found so far are biased toward luminous ones owing to observational limitations. It is widely known that for quasars, an anticorrelation was observed between an emission-line EW and luminosity, which is called the Baldwin effect (BEff; Baldwin 1977). First, we report the results of near-infrared spectroscopic observations of six luminous quasars at $z \sim 2.7$, and later we discuss how the influence of the BEff on our abundance diagnostics can be excluded. This will enable us to derive the chemical abundance of BLR clouds at a much higher redshift than that studied in Paper I.

The remainder of this paper is organized as follows. Our target selection and the details of observations are presented in Section 2. Data reduction including one-dimensional spectrum extraction and correction for telluric absorption is described in Section 3. The measurement of emission lines by fitting a spectral model to the observed spectrum is described in Section 4, and the results are summarized in Section 5. In Section 6, the investigation of the BEff for Mg II and Fe II emission lines using a large sample of Sloan Digital Sky Survey (SDSS) quasars is presented, and its relationship with the dependence on the Eddington ratio is discussed. Further, a method to correct the BEff to derive $[\text{Mg}/\text{Fe}]$ and $[\text{Fe}/\text{H}]$ is presented, and it is compared with the chemical evolution models in the redshift range of $0.7 < z < 2.7$. The paper is summarized in Section 7. Throughout this paper, we assume Λ CDM cosmology, with $\Omega_\Lambda = 0.7$, $\Omega_M = 0.3$, and $H_0 = 70 \text{ km s}^{-1} \text{ Mpc}^{-1}$.

2. TARGET SELECTION AND OBSERVATION

¹ $[\alpha/\text{Fe}] \equiv \log(n_\alpha/n_{\text{Fe}}) - \log(n_\alpha/n_{\text{Fe}})_\odot$, where n_x represents the number density of the element x ($= \alpha$ element or Fe). Throughout this paper, we will use this logarithmical expression for abundance ratios.

² A part of the variance is arguably due to the difference in the fitting procedures adopted. Therefore, it is advisable to obtain spectra of similar quality and analyze them in the same manner.

Target candidates were selected from the SDSS Data Release 12 (DR12) Quasar Catalog (Pâris et al. 2017). To avoid serious telluric absorption, the redshift range was restricted to approximately 2.7 so that the Mg II $\lambda 2798$ emission line would be located in the central region of the Y band (9760–11100 Å).

The observations were carried out in 2018 March using the WINERED echelle spectrograph (Ikeda et al. 2016) mounted on the ESO 3.58 m New Technology Telescope (NTT) at the La Silla Observatory, Chile (ESO program ID: 0100.B-0939(A)). The observation mode was set to the WIDE mode with a 200 μm width slit, which had a wavelength coverage of 0.90–1.35 μm and a resolving power of $R \sim 17000$. The targets were observed at two positions separated by approximately $10''$ along the slit by nodding the telescope to make the ABBA dithering sequence. Telluric standard stars were also observed before or after the targets so that the differences in time and airmass between them were as close as possible. Each night, HD 111844, an F-type star whose medium-resolution ($R \sim 2000$) spectrum was available at the IRTF Spectral Library³ (Rayner et al. 2009), was observed as the flux standard star. Finally, we observed six quasars (hereafter, NTT quasars), some of which were observed over multiple days. The observation log is summarized in Table 1.

Figure 1 shows the sample distribution of the NTT quasars in the absolute magnitude–redshift plane; the quasars included in the SDSS DR12 Quasar Catalog and those investigated in Paper I (hereafter, Paper I SDSS quasars) are also shown as reference. From this figure, it can be seen that the NTT quasars are much brighter than most Paper I SDSS quasars, and they are even located in the bright end of quasars with nearly the same redshift. This characteristic is suitable for investigating the BEff.

3. DATA REDUCTION

The observed data of the NTT quasars were reduced in a standard manner using IRAF⁴ routines as follows. First, sky subtraction was performed by taking the difference between two consecutive images taken at different slit positions, i.e., A–B and B–A. Then, scattered light was evaluated in the interorder regions of each difference image and was removed. Flat fielding was performed using a dome-flat image. The bad pixels

³ http://irtfweb.ifa.hawaii.edu/~spex/IRTF_Spectral_Library/

⁴ IRAF is distributed by the National Optical Astronomy Observatories, which are operated by the Association of Universities for Research in Astronomy, Inc., under cooperative agreement with the National Science Foundation.

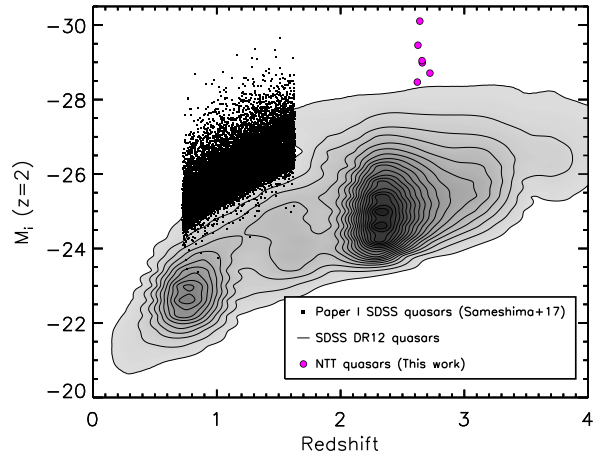


Figure 1. Sample distribution in the absolute magnitude–redshift plane for NTT quasars (magenta circle) and Paper I SDSS quasars (black dot). For reference, the distribution of all samples in the SDSS DR12 Quasar Catalog is shown by contours.

were masked and replaced through linear interpolation from the surrounding pixels. The spectral line tilts in the two-dimensional images were corrected by performing a geometrical transformation using arc-lamp images as reference. Then, one-dimensional spectra were extracted using the IRAF task `apall` for each order, and background subtraction was performed by using the sky region. Wavelength calibration was performed using the Th–Ar lamp spectra extracted in the same manner as the target object. Then, each frame spectrum observed on the same day was coadded.

The telluric absorption was corrected by using synthetic telluric spectra created by `molecfit` (Smette et al. 2015; Kausch et al. 2015) as follows. Because the signal-to-noise ratio (S/N) of the obtained quasar spectrum was not sufficient for the accurate estimation of the telluric absorption, we used the high-S/N spectrum of the corresponding telluric standard star instead. By running `molecfit` with the spectrum of the telluric standard star, we created a synthetic telluric spectrum and used it with the IRAF task `telluric` to correct the quasar spectrum for telluric absorption. An example of the correction for telluric absorption is illustrated in Figure 2.

The response curves were derived from the observed spectrum of the flux standard star HD 111844 that was corrected for telluric absorption in the same manner as quasars. These response curves were used for flux calibration to restore the true slopes of the quasar spectra. For quasars that were observed for multiple days, each flux-calibrated spectrum was scaled so that the median fluxes matched, and then they were coad-

Table 1. Summary of observation

Object	α (J2000.0)	δ (J2000.0)	z^a	J_{Vega}^b	WINERED				SDSS		
					Exposure	Airmass	Seeing ^c	Date	S/N ^d	Date ^e	S/N ^e
J0828+1251	08 28 57.22	+12 51 40.0	2.722	15.974	600 s \times 10	1.39–1.38	1.2	2018 Mar 4	7.1	2011 Jan 3	21.53
					600 s \times 6	1.39–1.53	0.9	2018 Mar 5			
J0850+1108	08 50 45.73	+11 08 40.5	2.620	16.470	900 s \times 2	1.33–1.32	1.8	2018 Mar 2	13.5	2012 Jan 21	22.31
					900 s \times 8	1.70–1.31	1.1	2018 Mar 3			
					900 s \times 8	1.55–1.31	1.0	2018 Mar 5			
					900 s \times 8	1.33–1.41	0.9	2018 Mar 6			
J1011+2941	10 11 55.59	+29 41 41.5	2.640	14.870	900 s \times 3	1.98–1.93	0.8	2018 Mar 3	12.6	2013 Feb 5	46.99
J1107+0436	11 07 08.41	+04 36 17.9	2.660	15.685	900 s \times 10	1.28–1.28	1.0	2018 Mar 4	22.1	2012 Jan 2	39.47
J1130+0732	11 30 17.37	+07 32 12.9	2.658	16.110	900 s \times 12	1.28–1.53	0.8	2018 Mar 6	15.2	2012 Jan 21	48.24
J1142+2654	11 42 54.26	+26 54 57.5	2.625	15.823	750 s \times 8	1.94–1.80	1.0	2018 Mar 2	16.2	2013 Feb 13	46.36
					900 s \times 4	1.86–1.79	1.3	2018 Mar 3			

^aRedshift from visual inspection (Z_VI) taken from the SDSS DR12 Quasar catalog (Pâris et al. 2017).

^b J -band magnitude (Vega) taken from the 2MASS All Sky Catalog of point sources (Cutri et al. 2003).

^cAverage seeing during the observation in the unit of arcsec.

^dMedian signal-to-noise ratio per pixel at the J band of the spectrum after coadding and rebinning.

^eTaken from the Sloan Digital Sky Survey III Science Archive Server (<https://dr12.sdss.org/>).

ded with weights according to the exposure time. Finally, the spectrum was rebinned by calculating the median of neighboring 13 or 14 pixels and scaled to match the corresponding low-resolution optical spectrum taken by SDSS at $\sim 1 \mu\text{m}$, assuming that the change of spectral shape during the time between the SDSS and WINERED observations was negligible. All the final spectra of the NTT quasars are shown in Figure 3, and their median S/Ns in the J band are listed in Table 1.

4. ANALYSIS

The fluxes of Mg II and Fe II emission lines were measured in the same manner as in Paper I. First, the following continuum model was fitted to the spectrum:

$$F_\lambda = F_\lambda^{\text{PL}}(\alpha, \beta) + F_\lambda^{\text{BaC}} + F_\lambda^{\text{FeII}}(\gamma), \quad (1)$$

where F_λ^{PL} is a power-law continuum flux emitted from an accretion disk, F_λ^{BaC} is a Balmer continuum flux, and F_λ^{FeII} is a Fe II pseudo-continuum flux. We adopted the Balmer continuum model proposed by Grandi (1982) for F_λ^{BaC} ; the shape and flux ratio against the power-law component were fixed as was done in previous works (e.g., De Rosa et al. 2011; Sameshima et al. 2017; Shin et al. 2019). We used the Fe II template given by Tsuzuki et al. (2006). Prior to fitting, the Fe II template was broadened by convolution with a Gaussian function,

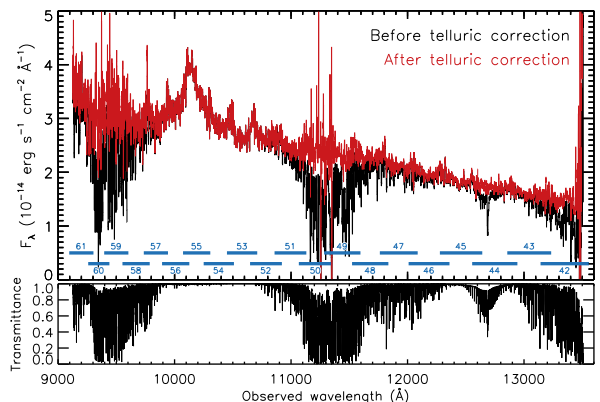


Figure 2. An example of correction for telluric absorption. In the upper panel, the spectra prior to (black) and after (red) telluric correction are shown with the free spectral ranges of echelle orders (blue). In the lower panel, a synthetic telluric spectrum created with `molecfit` is shown as reference.

for which the FWHM was fixed⁵ at 2000 km s^{-1} . Thus, there were three free parameters: the power-law slope (α), normalization of the power-law continuum flux (β), and normalization of the Fe II pseudo-continuum flux (γ). The best-fit parameters were obtained by perform-

⁵Note that, as De Rosa et al. (2011) pointed out, the FWHM adopted for the convolved Gaussian function has a negligible effect on the measured Fe II flux.

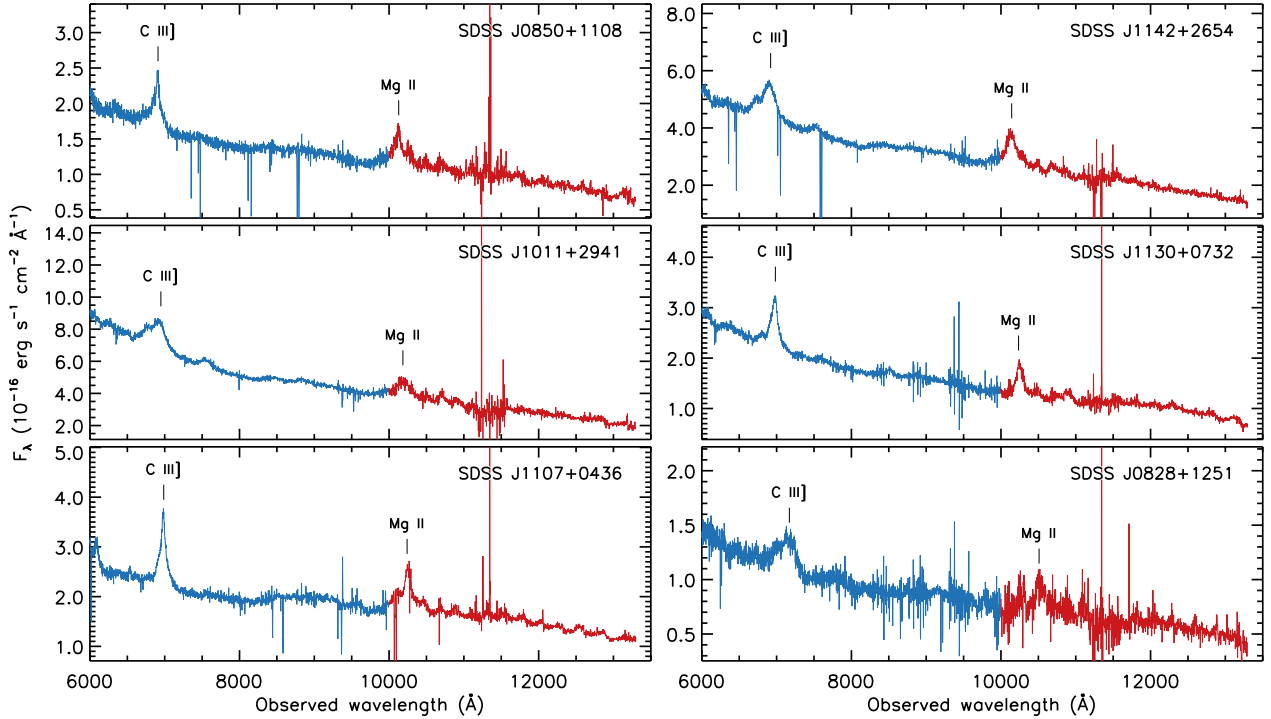


Figure 3. Observed spectra of NTT quasars. The blue line represents the archival SDSS spectrum, and the red line represents the WINERED spectrum that is rebinned and scaled to match the SDSS spectrum.

ing χ^2 minimization with the IDL procedure `MPFIT.pro` (Markwardt 2009). Fe II flux was calculated by integrating the fitted Fe II template in the wavelength range of 2200–3090 Å. Then, the Mg II $\lambda 2798$ emission line in the continuum-subtracted spectrum was fitted with one or two Gaussians with the `MPFIT.pro` procedure. For fitting with two Gaussians, both the flux and the FWHM of Mg II were calculated from the sum of the Gaussians. The rest-frame EWs of Fe II and Mg II emission lines were measured by dividing the line flux by the continuum flux density at 3000 Å. Examples of spectral fitting for the NTT quasars are shown in Figure 4.

The mass of a black hole (BH), M_{BH} , was estimated from the Mg II FWHM and the continuum luminosity at 3000 Å by using the virial mass estimate formula (Vestergaard & Osmer 2009):

$$\log\left(\frac{M_{\text{BH}}}{M_{\odot}}\right) = 6.86 + 2 \log\left(\frac{\text{FWHM}(\text{Mg II})}{1000 \text{ km s}^{-1}}\right) + 0.5 \log\left(\frac{\lambda L_{\lambda}(3000 \text{ \AA})}{10^{44} \text{ erg s}^{-1}}\right). \quad (2)$$

For a BLR cloud orbiting the central BH, the Eddington luminosity is given by

$$L_{\text{Edd}} = \frac{4\pi G c m_p}{\sigma_e} M_{\text{BH}}, \quad (3)$$

where G is the gravitational constant, c is the speed of light, m_p is the proton mass, and σ_e is the Thomson

scattering cross section (Peterson 1997). Following Shen et al. (2011), we estimated the bolometric luminosity from the measured monochromatic luminosity at 3000 Å with the bolometric correction formula:

$$L \equiv L_{\text{bol}} = 5.15 \lambda L_{\lambda}(3000 \text{ \AA}). \quad (4)$$

From equations (2)–(4), the Eddington ratio is written as

$$\log\left(\frac{L}{L_{\text{Edd}}}\right) = -0.249 - 2 \log\left(\frac{\text{FWHM}(\text{Mg II})}{1000 \text{ km s}^{-1}}\right) + 0.5 \log\left(\frac{\lambda L_{\lambda}(3000 \text{ \AA})}{10^{44} \text{ erg s}^{-1}}\right). \quad (5)$$

For all the NTT quasars, the Eddington ratio was evaluated using the above equation, as was done for the Paper I SDSS quasars.

The measurement errors were estimated through Monte Carlo simulations, similarly to the study of Shin et al. (2019). We performed the above fitting procedures for a set of 1000 mock spectra generated by randomizing the errors in each pixel of the observed spectrum. For each measured quantity, the median value of the mock spectra was adopted as the maximum likelihood estimate, and the interval between the 15.87th and 84.13th percentiles was adopted as the 1σ confidence interval. All measurements and errors of the NTT quasars calculated in this manner are summarized in Table 2.

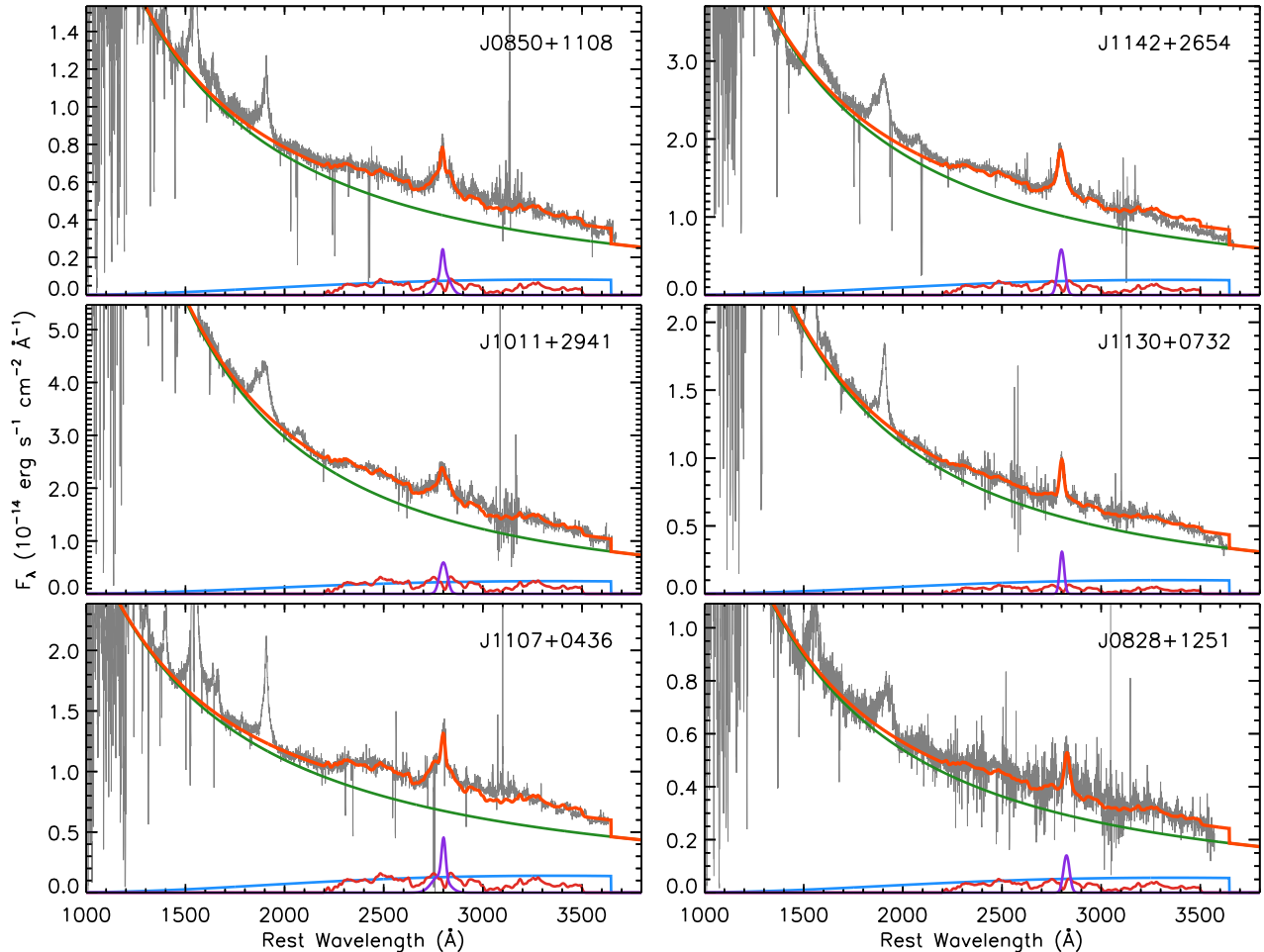


Figure 4. Results of spectral fitting for NTT quasars. The best-fit power-law continuum (green), Balmer continuum (blue), Fe II emission lines (red), Mg II emission line (purple), and their sum (orange) are overplotted on the observed spectrum (gray).

5. RESULTS

5.1. Luminosity and the Eddington ratio

Figure 5 shows the monochromatic luminosity L_{3000} ($\equiv \lambda L_{\lambda}(3000\text{\AA})$) and the Eddington ratio as a function of redshift for the six NTT quasars analyzed in this study, along with the Paper I SDSS quasars for comparison. The luminosity of the NTT quasars spans $10^{46.6} < L_{3000} < 10^{47.3}$ erg s $^{-1}$, which is considerably brighter than most Paper I SDSS quasars. Note that the WINERED spectrum was scaled to the corresponding SDSS DR12 spectrum obtained for the same object, but a few years earlier; therefore, the obtained values for the NTT quasars do not necessarily reflect luminosities in the observation period of WINERED, i.e., 2018 March. The Eddington ratios of NTT quasars are systematically greater than those of Paper I SDSS quasars, which is mainly due to the brightness. Further, almost

all NTT quasars fulfill $L/L_{\text{Edd}} \gtrsim 1$, suggesting that they are likely to be super-Eddington objects.

5.2. Fe II/Mg II fluxes

Figure 6 shows the EW(Fe II), EW(Mg II), and Fe II/Mg II flux ratio⁶ as a function of redshift, along with the Paper I SDSS quasars as reference. Note that the EWs were measured in their rest frames. For all the three parameters, the dynamic range of the measured values approximately match for the two samples, despite the large difference in luminosity. This suggests that there is no evolution of the Fe II/Mg II flux ratio over a long period of cosmic time, which is consistent with the results and observations of previous studies (e.g.,

⁶ Here, the flux ratio Fe II/Mg II equals the equivalent-width ratio $\text{EW}(\text{Fe II})/\text{EW}(\text{Mg II})$, because we used the common continuum flux at 3000 Å for calculating EW(Fe II) and EW(Mg II) as described in §4.

Table 2. Results of fitting

Object	$z_{\text{Mg II}}^a$	FWHM (km s ⁻¹)	EW(Mg II) ^b (Å)	EW(Fe II) ^b (Å)	Fe II/Mg II	$\log L_{3000}^c$ (erg s ⁻¹)	$\log M_{\text{BH}}/M_{\odot}$	$\log L/L_{\text{Edd}}$
J0828+1251	2.758 ^{+0.003} _{-0.002}	4400 ⁺⁴⁶⁰ ₋₄₀₀	18.1 ^{+1.5} _{-1.5}	75.9 ^{+6.5} _{-6.1}	4.21 ^{+0.56} _{-0.50}	46.638 ^{+0.003} _{-0.003}	9.47 ^{+0.09} _{-0.08}	-0.13 ^{+0.17} _{-0.18}
J0850+1108	2.617 ^{+0.002} _{-0.002}	4080 ⁺⁴⁹⁰ ₋₅₄₀	29.7 ^{+1.3} _{-1.3}	99.1 ^{+3.7} _{-3.4}	3.33 ^{+0.21} _{-0.19}	46.758 ^{+0.002} _{-0.002}	9.46 ^{+0.10} _{-0.12}	-0.09 ^{+0.12} _{-0.10}
J1011+2941	2.644 ^{+0.002} _{-0.002}	5040 ⁺²⁸⁰ ₋₂₈₀	19.9 ^{+1.0} _{-1.0}	111.4 ^{+2.8} _{-3.0}	5.60 ^{+0.32} _{-0.31}	47.272 ^{+0.002} _{-0.002}	9.90 ^{+0.05} _{-0.05}	-0.02 ^{+0.05} _{-0.05}
J1107+0436	2.666 ^{+0.001} _{-0.001}	3000 ⁺¹⁸⁰ ₋₁₇₀	37.1 ^{+10.6} _{-4.4}	111.9 ^{+2.9} _{-3.4}	2.97 ^{+0.48} _{-0.68}	46.981 ^{+0.002} _{-0.003}	9.30 ^{+0.05} _{-0.05}	+0.29 ^{+0.05} _{-0.05}
J1130+0732	2.664 ^{+0.001} _{-0.001}	2780 ⁺¹¹⁰ ₋₁₁₀	15.4 ^{+0.6} _{-0.7}	72.4 ^{+2.8} _{-2.7}	4.71 ^{+0.29} _{-0.25}	46.875 ^{+0.001} _{-0.002}	9.18 ^{+0.03} _{-0.04}	+0.30 ^{+0.03} _{-0.03}
J1142+2654	2.625 ^{+0.001} _{-0.001}	4650 ⁺¹⁷⁰ ₋₁₅₀	23.7 ^{+0.7} _{-0.7}	84.7 ^{+1.9} _{-1.9}	3.59 ^{+0.13} _{-0.14}	47.144 ^{+0.001} _{-0.001}	9.77 ^{+0.03} _{-0.03}	-0.01 ^{+0.03} _{-0.03}

^aRedshift obtained from the fitting of the Mg II emission line.

^bEWs are measured in the rest-frame wavelength.

^c $L_{3000} \equiv \lambda L_{\lambda}(3000\text{Å})$.

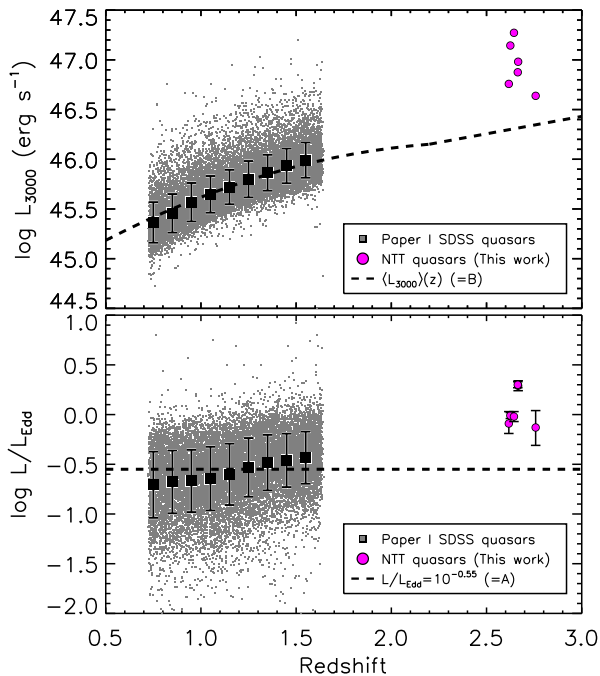


Figure 5. Distribution of the six NTT quasars at $z \sim 2.7$ (magenta circle) and the Paper I data (gray dots) on the $\log L_{3000}-z$ plane (top panel) and $\log L/L_{\text{Edd}}-z$ plane (bottom panel). The dashed lines represent the fiducial values B and A , which are discussed in §6.4.

De Rosa et al. 2011, 2014; Mazzucchelli et al. 2017; Shin et al. 2019).

6. DISCUSSION

6.1. Baldwin effect and metallicity

Baldwin (1977) found that the EW of C IV $\lambda 1549$ emission line is anticorrelated with continuum luminosity in AGNs, which is now called the BEff. A similar anticorrelation was soon found for Mg II $\lambda 2798$ (Bald-

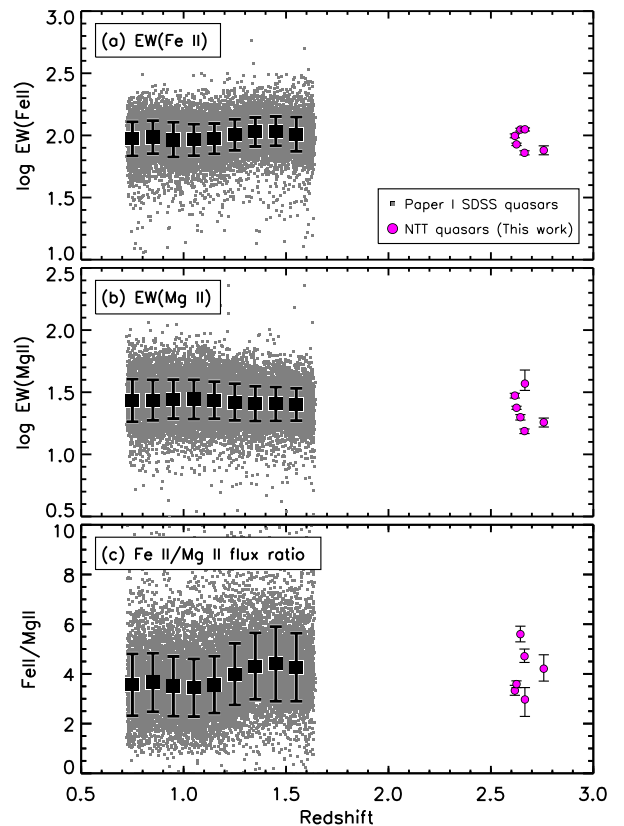


Figure 6. (a) EW(Fe II), (b) EW(Mg II), and (c) Fe II/Mg II flux ratio as a function of redshift for the six NTT quasars at $z \sim 2.7$ (magenta circle) and Paper I SDSS quasars (gray dots). For the latter data, the mean values and standard deviations (after 3σ clipping) in each redshift bin ($\Delta z = 0.15$) are represented by filled boxes and error bars, respectively.

win et al. 1978). Currently, this effect has been detected for almost all UV and optical emission lines of AGNs, including Mg II and Fe II (e.g., Laor et al. 1995; Osmer

& Shields 1999; Dietrich et al. 2002b; Shields 2007). An intriguing aspect reported by Dietrich et al. (2002b) is that the slope, measured as $EW \propto (\lambda L_\lambda)^\beta$, becomes steeper as the ionization energy of the line increases. Further, Xu et al. (2008) reported that the slope index β for C IV $\lambda 1549$ seems to be independent of the redshift up to $z \sim 5$.

While there is no doubt that the BEff exists from an observational perspective, its physical origin remains an open question. Several scenarios have been proposed for this so far, such as (1) a luminosity-dependent ionization parameter (Mushotzky & Ferland 1984), (2) an orientation-dependent anisotropic continuum with a more isotropic line emission (Netzer 1985), and (3) a luminosity-dependent continuum spectral energy distribution (SED; Korista et al. 1998; Dietrich et al. 2002b).

Given that the BEff has been detected even for hydrogen and helium lines (e.g., Laor et al. 1995; Dietrich et al. 2002b), there is some evidence to conclude that its main cause is not metallicity. This argument may be supported by observations of metallicity-sensitive nitrogen emission lines. Jiang et al. (2008) found that $\sim 1.1\%$ of their quasar sample retrieved from SDSS DR5 have strong N V $\lambda 1240$, N IV] $\lambda 1486$, and N III] $\lambda 1750$ emission lines. These quasars are very likely to have a large nitrogen abundance. However, they reported that the difference in luminosity between these quasars with strong nitrogen emission lines and normal quasars is too small to explain the BEff.

On the other hand, Korista et al. (1998) argued metallicity as a second driver of the BEff based on the fact that the BEff is not seen in N V $\lambda 1240$. Their photoionization calculation showed that the EWs of various emission lines, including N V, are weaker for softer ionizing continua. This result indicates that the luminosity dependence of the SED, which becomes softer as the object becomes brighter, is the primary driver of the BEff. Then, Korista et al. (1998) argued that if metallicity in addition to the softness of the SED increases as the luminosity increases, the decrease of $EW(\text{N V})$ due to the SED can be compensated by the rapid increase of N V due to metallicity, which can reproduce the observations. Warner et al. (2003, 2004) showed that the BEff can be reproduced by using the BH mass instead of luminosity. They also estimated the metallicity from line ratios including N V following the method of Hamann et al. (2002) and showed that there is a relationship between the BH mass and BLR metallicity. This may suggest that the BEff is related to the mass-metallicity relationship found in galaxies. However, it should be noted that these results were obtained based on N V and do not necessarily agree with the results of other nitrogen

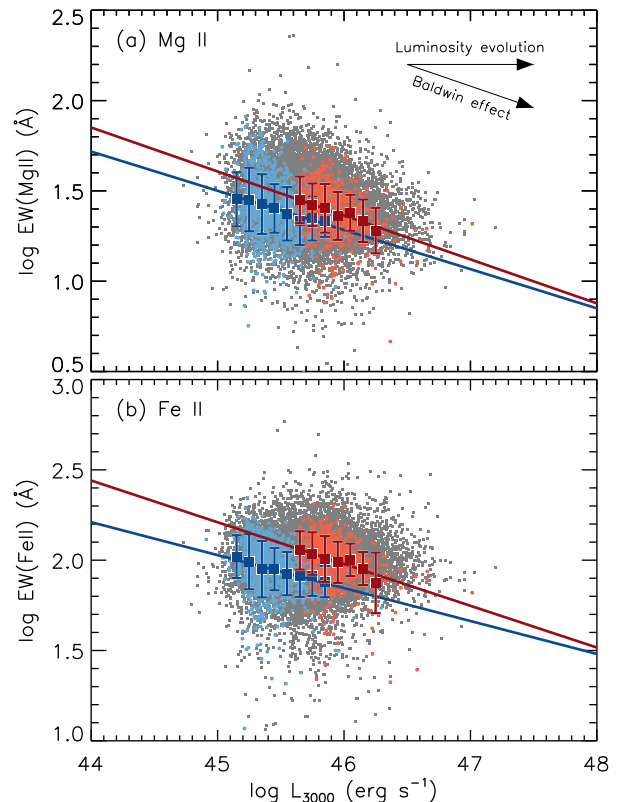


Figure 7. Distribution of Paper I data on the EW– $\log L_{3000}$ plane for (a) Mg II and (b) Fe II. Gray dots are Paper I data with $\chi^2_\nu < 1.2$ at $0.72 < z < 1.63$. Redshift-binned subsamples ($0.8 < z < 0.9$ with blue circles; $1.4 < z < 1.5$ with red circles) are also shown. The solid lines indicate regression lines of the two subsamples.

emission lines. Dietrich et al. (2002b) detected the BEff for N III] $\lambda 1750$ and N IV] $\lambda 1486$, unlike N V. Warner et al. (2003) found no trend between the BH mass and metallicity when N III] instead of N V was used as an indicator of metallicity.

Given this indeterminacy of different results for different nitrogen emission lines as well as the plausibility that the luminosity-dependent SED is the primary driver, we consider the BEff to be independent of chemical abundances in this study, and will correct measured EWs for the BEff before abundance estimate.

6.2. Baldwin effect for Mg II and Fe II

Here, we investigate the BEff for Mg II and Fe II emission lines using the Paper I SDSS quasars, which have a sufficient sample size. Figure 7 shows the distribution of the Paper I SDSS quasars in the EW– L_{3000} diagram for Mg II and Fe II. Because the Paper I SDSS quasars are basically flux-limited ($i = 19.1$ for $z \lesssim 3$ quasars; see Schneider et al. 2010) and the limiting luminosity accordingly depends on the redshift, we divided

Table 3. Correlation between EW and L_{3000}

Redshift Range	EW(Mg II)			EW(Fe II)			N_{obj}
	Slope	ρ^\dagger	p^\ddagger	Slope	ρ^\dagger	p^\ddagger	
Redshift-binned subsamples							
$0.7 < z < 0.8$	-0.17	-0.17	5×10^{-7}	-0.12	-0.15	1×10^{-5}	851
$0.8 < z < 0.9$	-0.22	-0.25	3×10^{-17}	-0.18	-0.27	5×10^{-20}	1089
$0.9 < z < 1.0$	-0.20	-0.20	2×10^{-10}	-0.22	-0.29	8×10^{-20}	971
$1.0 < z < 1.1$	-0.26	-0.26	7×10^{-17}	-0.19	-0.27	4×10^{-18}	1016
$1.1 < z < 1.2$	-0.27	-0.28	1×10^{-16}	-0.21	-0.28	3×10^{-16}	853
$1.2 < z < 1.3$	-0.29	-0.32	5×10^{-19}	-0.25	-0.29	3×10^{-16}	746
$1.3 < z < 1.4$	-0.21	-0.23	9×10^{-10}	-0.20	-0.26	9×10^{-12}	678
$1.4 < z < 1.5$	-0.24	-0.28	8×10^{-13}	-0.23	-0.29	5×10^{-14}	648
$1.5 < z < 1.6$	-0.28	-0.31	3×10^{-16}	-0.18	-0.24	2×10^{-10}	662
All sample							
$0.72 < z < 1.63$	-0.13	-0.21	$< 1 \times 10^{-30}$	-0.02	-0.03	0.02	7710

† Spearman’s rank correlation coefficient.

‡ p -value for a null hypothesis that there is no correlation.

them into redshift-binned subsamples. As an example, two redshift-binned subsamples of $0.8 < z < 0.9$ and $1.4 < z < 1.5$ are plotted in different colors for clarity in Figure 7. Note that quasars at lower luminosity are missing because of the flux limit of observation. Table 3 summarizes the correlation analysis results. Although the luminosity range of each redshift-binned subsamples is narrow (~ 0.5 dex), anticorrelation was confirmed with the p -value $\leq 10^{-5}$ for each subsample for both Mg II and Fe II. The slope index β was in the range of -0.17 to -0.29 with $\langle \beta \rangle = -0.24$ for Mg II, while -0.12 to -0.25 with $\langle \beta \rangle = -0.21$ for Fe II. A relatively large scatter was observed for the values of β ; however, no particular redshift trend was observed, which is consistent with the result for C IV reported by Xu et al. (2008).

In Figure 7, a horizontal shift of the distribution can be observed between the two redshift-binned subsamples. As studies on the luminosity function indicate, quasars show a drastic luminosity evolution at $z \lesssim 2$ (e.g., Boyle et al. 1988; Croom et al. 2009; Ross et al. 2013), which results in this horizontal shift. When subsamples with the same slope index β are shifted horizontally, the slope of the whole sample becomes shallow. As a consequence, the BEff may be weakened or hidden by the luminosity evolution of quasars when a whole sample with a wide range of redshift is used to plot an EW– L_{3000} diagram. When Paper I SDSS quasars were used regardless of the redshift, we found little or no correlation between the EW and the luminosity for Fe II (see Table 3). As another example, Xu et al. (2008) reported that the slope of the C IV BEff is steeper for their redshift-binned

subsample than for the whole sample; this is naturally expected if quasars of whole samples covering a wide range of redshift ($1.5 \lesssim z \lesssim 5.1$) underwent luminosity evolution. Thus, it is important to make subsamples in the redshift to separate the luminosity evolution effect from the BEff.

6.3. Relationship between the dependence on the Eddington ratio and the Baldwin effect

As discussed in Paper I, the EWs of Mg II and Fe II are correlated with the Eddington ratio, which is a parameter that mainly affects the observable properties of quasars (Boroson 2002). The following question now arises: does the BEff possibly arise due to the dependence of the EW on the Eddington ratio? Dong et al. (2009) investigated this point for Mg II. They analyzed the spectroscopic data of Seyfert 1 galaxies and quasars at $0.45 \leq z \leq 0.8$ retrieved from SDSS DR4, and they found a strong negative correlation between EW(Mg II) and L/L_{Edd} . Furthermore, they found no correlation between EW(Mg II) and luminosity for their sample for the same L/L_{Edd} . Therefore, they concluded that the BEff is purely the secondary effect of the EW– L/L_{Edd} relationship. Here, we extend their study to include higher redshift data and investigate both Mg II and Fe II.

We performed a two-dimensional least-squares fitting in the log scale, where L/L_{Edd} and L_{3000} were simultaneously taken as independent variables, i.e.,

$$\log \text{EW} = \alpha \log \left(\frac{L/L_{\text{Edd}}}{A} \right) + \beta \log \left(\frac{L_{3000}}{B} \right) + \gamma, \quad (6)$$

where α and β are the slope indices of the dependence on the Eddington ratio and the BEff, respectively, and A and B are the fiducial values of the independent variables. Given that both the dependence on the Eddington ratio and the BEff are independent to the chemical composition of the gas, the constant γ is expected to strongly reflect the abundance.

In this study, we adopted the typical measured values for quasars as the fiducial values A and B , taking the following abundance estimate into account. As the dependence of the Eddington ratio on redshift is only slight at $0.7 \lesssim z \lesssim 1.6$ (see Figure 5), we adopted a constant value as the fiducial value of the Eddington ratio:

$$A = 10^{-0.55}, \quad (7)$$

which was retrieved from the median value of the whole Paper I SDSS quasars, as was done in Paper I.

To determine the fiducial value of luminosity B , we referred to studies on the quasar luminosity function. [Ross et al. \(2013\)](#) measured the luminosity functions of quasars using data from the SDSS-III Baryon Oscillation Spectroscopic Survey; they found that the measured luminosity functions can be fitted with a pure luminosity evolution model at $0.3 < z < 2.2$, whereas a luminosity evolution density evolution model is needed at $2.2 < z < 3.5$. Following their parameterization, the characteristic (or break) absolute magnitude is written as

$$M_i^*(z) = \begin{cases} M_i^*(0) - 2.5(k_1 z - k_2 z^2) & (0.3 < z < 2.2) \\ M_i^*(2.2) + c_2(z - 2.2) & (2.2 < z < 3.5), \end{cases} \quad (8)$$

where $M_i^*(z)$ is the absolute magnitude at which the faint-end and bright-end slopes of a luminosity function at redshift z overlap, $k_1 = 1.241$, $k_2 = -0.249$, and $c_2 = -0.875$. This equation can be written equivalently in terms of luminosity as

$$\log L^*(z) = \begin{cases} \log L^*(0) + k_1 z - k_2 z^2 & (0.3 < z < 2.2) \\ \log L^*(2.2) - (c_2/2.5)(z - 2.2) & (2.2 < z < 3.5). \end{cases} \quad (9)$$

Assuming that typical monochromatic luminosity $\langle L_{3000} \rangle$ also changes with redshift as in Equation (9), we determine the zero-point by minimizing χ_ν^2 for the Paper I SDSS quasars and derive $\langle L_{3000} \rangle(z=0) = 10^{44.63}$ erg s⁻¹. The typical luminosity $\langle L_{3000} \rangle(z)$ thus determined is plotted as a function of redshift in Figure 5; it is evident that $\langle L_{3000} \rangle(z)$ agrees with the distribution of Paper I data very well and is suitable for the fiducial luminosity. Therefore, we adopt $\langle L_{3000} \rangle(z)$ as the fiducial

value B in Equation (6), i.e.,

$$B = \begin{cases} 10^{44.63} + 1.241z + 0.249z^2 & (0.3 < z < 2.2) \\ 10^{46.15} + 0.350(z - 2.2) & (2.2 < z < 3.5), \end{cases} \quad (10)$$

in the unit of erg s⁻¹.

By using Equation (6) with the above A and B , we performed a simultaneous fitting of EWs; the results are shown in Figure 8. Notable characteristics of the fitting are summarized as follows:

1. α and β clearly show different patterns between Mg II and Fe II, even though they have similar ionization potential.
2. The slope index of the Eddington ratio α shows little or no dependence on redshift. The values are almost consistent with the results of Paper I for both Mg II and Fe II.
3. The slope index of luminosity β may depend on redshift. Generally, the higher the redshift, the steeper the slope for both Mg II and Fe II.
4. γ is approximately constant for redshifts for both Mg II and Fe II. This is consistent with the theoretical expectations of the chemical evolution models that the chemical abundance of the gas was nearly constant at $0.7 \lesssim z \lesssim 1.6$.

Our result shows that $\beta(\text{Mg II})$ is almost zero at $z \lesssim 1.5$, implying no correlation between EW(Mg II) and luminosity, which is consistent with the argument proposed by [Dong et al. \(2009\)](#). However, at $z \gtrsim 1.5$, which was not investigated by [Dong et al. \(2009\)](#), $\beta(\text{Mg II})$ becomes nonzero. Furthermore, $\beta(\text{Fe II})$ is nonzero regardless of redshift. These results indicate that the BEff is more than a secondary effect in the EW(Mg II)- L/L_{Edd} relationship. The different redshift dependences of α and β shown in Figure 8 also suggest that the two effects are independent to some extent. This idea may be supported by the principal component analysis of the quasar spectra, which was performed by [Shang et al. \(2003\)](#); they found that the first principal component represents the BEff, while the third principal component is directly related to ‘‘Eigenvector 1’’ ([Boroson & Green 1992](#); [Sulentic et al. 2000](#)), which is thought to be mainly driven by the Eddington ratio ([Boroson 2002](#))⁷.

Further investigation of the difference between the BEff and the dependence on the Eddington ratio may

⁷ For reference, the second principal component derived by [Shang et al. \(2003\)](#) represents the UV continuum slope variation in quasar spectra.

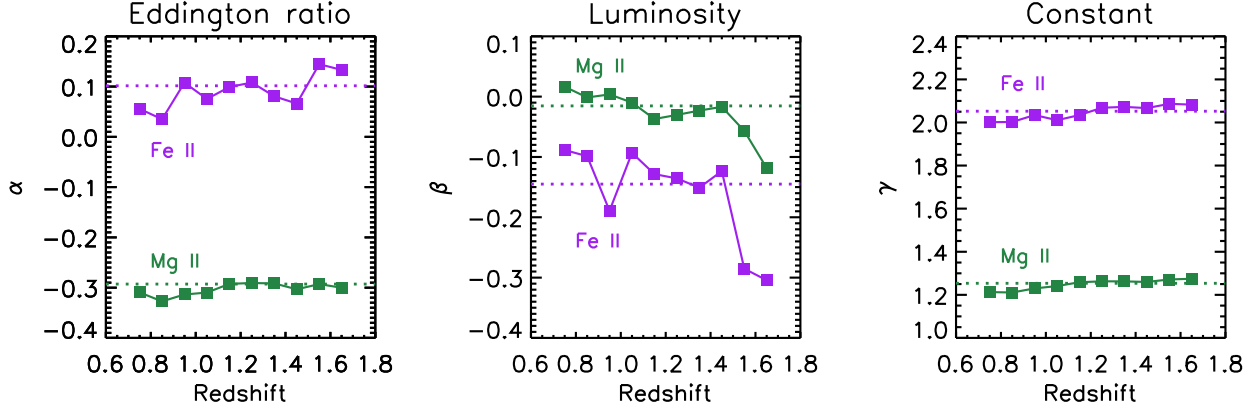


Figure 8. Parameters retrieved from the simultaneous fitting of EW with Equation (6) as a function of redshift for Mg II (green) and Fe II (purple). Dashed lines represent the results of the fitting using the whole sample; $(\alpha, \beta, \gamma) = (-0.29, -0.02, +1.25)$ for Mg II, and $(+0.10, -0.15, +2.05)$ for Fe II.

be helpful for solving long-standing issues regarding the BEff and for understanding the physical mechanisms of quasars. These topics are beyond the scope of this paper.

6.4. Abundance estimate

Given that there are observational results supporting that the BEff is not related to metallicity (see §6.1, e.g., Laor et al. 1995; Dietrich et al. 2002b), in addition to correcting for their dependence on the Eddington ratio, it is necessary to correct the measured EWs for the BEff to estimate the chemical abundance of a BLR cloud. This is especially important for most high-redshift quasars found thus far, including the NTT quasars analyzed in this study, because they are extraordinarily luminous compared with typical quasars at similar redshift. Thus, their EWs could be smaller than those of typical quasars due to the BEff. Here, we attempted to correct the measured EWs for the BEff in addition to the dependence on the Eddington ratio and estimated their chemical abundances by using the method described in Paper I.

Following the discussion in the previous section, we can derive an EW correction formula for the dependence on nonabundance factors:

$$EW' = EW \left(\frac{L/L_{\text{Edd}}}{A} \right)^{-\alpha} \left(\frac{L_{3000}}{B} \right)^{-\beta}, \quad (11)$$

where EW is the measured EW, and A and B are given in Equations (7) and (10), respectively. Figure 8 implies that α does not depend on redshift; therefore, we can safely adopt the value retrieved from the fitting result using the whole sample in the previous section (see Figure 8), i.e., $\alpha = -0.29$ (Mg II) and $+0.10$ (Fe II). In contrast, β may depend on redshift; however, sufficient data is not available for $z \gtrsim 1.6$. In this study, we con-

sidered the following two working hypotheses to derive the chemical abundances of the NTT quasars:

1. WH1: β does not depend on redshift. We adopt $\beta = -0.02$ for Mg II and -0.15 for Fe II (see the caption of Figure 8), which are retrieved from the fitting result using the whole sample in the same manner as α .
2. WH2: β depends on redshift. We adopt the same β as WH1 at $z < 1.5$, but adopt $\beta = -0.10$ for Mg II and -0.30 for Fe II at $z \geq 1.5$, which are inferred from Figure 8.

Figure 9 shows the abundance diagnostic diagram introduced in Paper I, where the calculated variation in $EW(\text{Mg II})$ and $EW(\text{Fe II})$ as functions of $[\text{Mg}/\text{Fe}]$ and $[\text{Fe}/\text{H}]$ is compared with the measured EWs of the NTT quasars and Paper I SDSS quasars after correction for the nonabundance factors. To check the effect of additional correction for the BEff, we have plotted three patterns: measured EWs corrected for only L/L_{Edd} with the Paper I method (top panel), and those corrected for both L/L_{Edd} and L_{3000} using Equation (11) with WH1 (middle panel) and WH2 (bottom panel). The derived $[\text{Mg}/\text{Fe}]$ and $[\text{Fe}/\text{H}]$ for these three cases are shown as a function of the age of the universe in Figure 10. The numerical values for these cases are listed in Table 4. Because the sample size of the Paper I SDSS quasars is large, the mean and standard deviation are calculated in each redshift bin ($\Delta z = 0.15$) and plotted in this figure. Similarly, the six NTT quasars are treated as one group and their weighted mean and standard deviation are plotted for proper comparison.

In Figure 10, the Paper I SDSS quasars at $z < 2$ are almost unaffected by the additional correction for the BEff. This is because the luminosity difference

Table 4. Derived abundances

Redshift Range	Corrected for L/L_{Edd} (Paper I method)		Corrected for L/L_{Edd} and L_{3000} (WH1)		Corrected for L/L_{Edd} and L_{3000} (WH2)	
	[Mg/Fe]	[Fe/H]	[Mg/Fe]	[Fe/H]	[Mg/Fe]	[Fe/H]
Paper I SDSS quasars						
$0.60 < z < 0.75$	-0.22 ± 0.34	$+0.27 \pm 0.55$	-0.27 ± 0.30	$+0.34 \pm 0.54$	-0.27 ± 0.30	$+0.34 \pm 0.54$
$0.75 < z < 0.90$	-0.23 ± 0.34	$+0.32 \pm 0.54$	-0.27 ± 0.34	$+0.37 \pm 0.56$	-0.27 ± 0.34	$+0.37 \pm 0.56$
$0.90 < z < 1.05$	-0.17 ± 0.30	$+0.26 \pm 0.51$	-0.22 ± 0.31	$+0.33 \pm 0.51$	-0.22 ± 0.31	$+0.33 \pm 0.51$
$1.05 < z < 1.20$	-0.16 ± 0.27	$+0.26 \pm 0.46$	-0.20 ± 0.24	$+0.32 \pm 0.45$	-0.20 ± 0.24	$+0.32 \pm 0.45$
$1.20 < z < 1.35$	-0.32 ± 0.24	$+0.47 \pm 0.43$	-0.34 ± 0.21	$+0.50 \pm 0.41$	-0.34 ± 0.21	$+0.50 \pm 0.41$
$1.35 < z < 1.50$	-0.36 ± 0.30	$+0.56 \pm 0.45$	-0.36 ± 0.28	$+0.56 \pm 0.44$	-0.36 ± 0.28	$+0.56 \pm 0.44$
$1.50 < z < 1.65$	-0.29 ± 0.33	$+0.46 \pm 0.47$	-0.29 ± 0.30	$+0.46 \pm 0.46$	-0.29 ± 0.30	$+0.47 \pm 0.45$
NTT quasars						
$2.61 < z < 2.76$	$+0.28 \pm 0.39$	$+0.06 \pm 0.33$	-0.16 ± 0.42	$+0.49 \pm 0.45$	-0.39 ± 0.45	$+0.96 \pm 0.62$

from the fiducial value, written as $\Delta \log L \equiv \log L_{3000} - \log \langle L_{3000} \rangle(z)$, is less than ± 0.25 dex for 68% of the sample; this changes the EW(Fe II) by less than $\pm 10\%$ with the assumption $\beta = -0.30$. In contrast, all the NTT quasars are more luminous than $\langle L_{3000} \rangle(z)$ with the mean difference $\langle \Delta \log L \rangle = +0.6$ dex; this changes the EW(Fe II) by approximately -50% with the assumption $\beta = -0.30$. Therefore, the derived abundances are almost unaffected for the Paper I SDSS quasars. This implies that the conclusions of Paper I are unchanged.

Further, the result for the NTT quasars at $z \sim 2.7$ depends on whether the measured EWs have been corrected properly for the nonabundance parameters, especially at $z \gtrsim 1.5$ where the slope change of the BEff is shown in the middle panel of Figure 8. When only the dependence on the Eddington ratio is corrected using the Paper I method (top panels of Figure 10), the derived [Mg/Fe] at $z \sim 2.7$ is greater than that obtained in Paper I, while the derived [Fe/H] at $z \sim 2.7$ is smaller than that in Paper I. The comparison of these results with those of the chemical evolution models (Yoshii et al. 1996, 1998) shows that the initial star formation redshift of $z_f = 5$ is required to reproduce the observation, which is clearly inconsistent with the existence of quasars at $z > 5$. In contrast, when additional correction is applied for the BEff, the derived [Mg/Fe] and [Fe/H] become more consistent with the models for $z_f = 10$ (middle panels of Figure 10), which are considered more appropriate according to our current knowledge about most distant objects in the universe. In particular, if we adopt WH2 (bottom panels of Figure 10), the derived [Mg/Fe] and [Fe/H] agree well with the models for $z_f = 10$. Although it is too early to put constraints on z_f given the limited number of the NTT quasars, the above results imply the following: (1) correction for the BEff in addi-

tion to the dependence on the Eddington ratio is needed to derive Mg and Fe abundances and their ratio from the measured EWs of Mg II and Fe II emission lines, and (2) the slope index of the BEff after separating the correction for the Eddington ratio likely evolves with redshift.

Our findings will be important for extending the chemical evolution studies using EWs of Mg II and Fe II emission lines of most distance quasars. However, further verification of our working hypotheses, i.e., whether the correlation slope of the BEff for Mg II and Fe II emission lines evolves even at $z \gtrsim 2$ is essential. This investigation will require a large sample of high-redshift quasars with sufficient dynamic range of luminosity. This will be implemented by using existing large telescopes (Subaru, VLT, Keck, etc.) as well as an upcoming 6.5 m infrared-optimized telescope in Chile constructed by The University of Tokyo Atacama Observatory (TAO) project (Yoshii et al. 2002, 2014, 2016; Doi et al. 2018).

7. SUMMARY

We performed near-infrared spectroscopy for luminous six quasars at $z \sim 2.7$ with the WINERED spectrograph mounted on the NTT at the La Silla Observatory, Chile. By combining these spectra with the optical spectra obtained by SDSS, we measured the EWs of Mg II and Fe II emission lines using the same method as in Paper I (Sameshima et al. 2017). The measured Fe II/Mg II flux ratios showed no significant change compared with those at $0.7 \lesssim z \lesssim 1.6$ (Figure 6), which is consistent with the results of previous studies, which argued that there was no redshift evolution of the Fe II/Mg II flux ratio.

From the analysis of Paper I SDSS quasars, we found the BEff, i.e., EW and luminosity are anticorrelated for both Mg II and Fe II emission lines (Figure 7). The two-dimensional least-squares fitting of measured EWs,

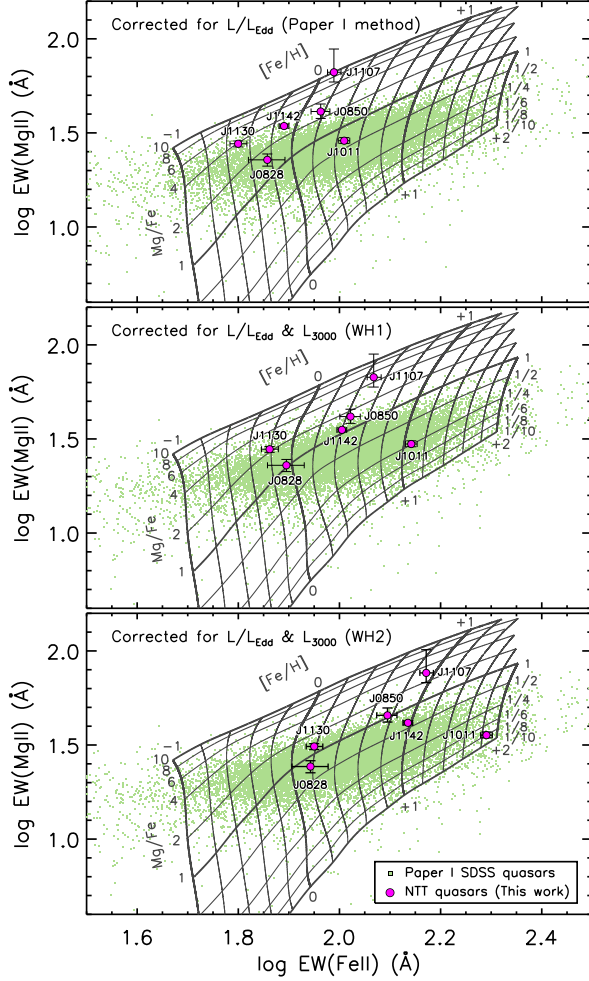


Figure 9. Calculated variation of $\text{EW}(\text{Mg II})$ and $\text{EW}(\text{Fe II})$ as functions of Mg/Fe ($= 10^{[\text{Mg}/\text{Fe}]}$) and $[\text{Fe}/\text{H}]$ (grid lines). The measured EWs corrected for only L/L_{Edd} (top panel), for both L/L_{Edd} and L_{3000} with WH1 (middle panel), and that with WH2 (bottom panel) are plotted for NTT quasars (magenta circle) and Paper I SDSS quasars (gray dot).

which incorporates the effect of quasar evolution inferred from a recent study on quasar luminosity function, indicated that the BEff and the dependence on the Eddington ratio are independent to some extent. The correlation slope index β of the BEff showed the feature of redshift evolution (Figure 8).

Based on previous studies supporting that the BEff does not represent metallicity, we corrected the measured EWs for the BEff in addition to the dependence on the Eddington ratio, which was done in Paper I. For the correction of EWs for the BEff , we assumed two working hypotheses that the slope index β does not evolve or evolves with redshift. By comparing these corrected EWs with those calculated through photoionization sim-

ulations in which the chemical abundance pattern of a BLR cloud was varied, we derived $[\text{Mg}/\text{Fe}]$ and $[\text{Fe}/\text{H}]$ for the NTT quasars and Paper I SDSS quasars (Table 4). We found that both the derived $[\text{Mg}/\text{Fe}]$ and $[\text{Fe}/\text{H}]$ were consistent with the prediction of chemical evolution models at $0.7 \lesssim z \lesssim 2.7$ when the additional correction for the BEff with redshift-dependent β is applied (Figure 10). This validates our method of flux-to-abundance conversion.

In the future, increasing the sample size of high-redshift quasars with sufficient dynamic range of luminosity is important for investigating the BEff at high redshift. This will be implemented by using large telescopes including an upcoming 6.5 m infrared-optimized telescope developed by the TAO project.

ACKNOWLEDGMENTS

We acknowledge the anonymous referee for constructive comments that helped improve the quality of our manuscript. We are grateful to the staff of the Koyama Astronomical Observatory for their support during our observation. We also thank Takuji Tsujimoto and Masao Mori for useful discussion. H.S. is supported by the Japan Society for the Promotion of Science (JSPS) KAKENHI grant No. 19K03917. The travel expenses to perform observation at NTT were supported by the Hayakawa Satio Fund in the Astronomical Society of Japan. WINERED was developed by the University of Tokyo and the Laboratory of Infrared High-resolution spectroscopy (LiH), Kyoto Sangyo University under the financial supports of Grants-in-Aid, KAKENHI, from JSPS (Nos. 16684001, 20340042, and 21840052) and the MEXT Supported Program for the Strategic Research Foundation at Private Universities (Nos. S081061 and S1411028). N.K. is supported by JSPS-DST under the Japan-India Science Cooperative Programs during 2013–2015 and 2016–2018. S.H. is supported by Grant-in-Aid for JSPS Fellows grant No. 13J10504. M.M. is supported by the Hakubi project at Kyoto University. K.F. is supported by KAKENHI (16H07323) Grant-in-Aid for Research Activity start-up.

Funding for SDSS-III has been provided by the Alfred P. Sloan Foundation, the Participating Institutions, the National Science Foundation, and the U.S. Department of Energy Office of Science. The SDSS-III website is <http://www.sdss3.org/>.

SDSS-III is managed by the Astrophysical Research Consortium for the Participating Institutions of the SDSS-III Collaboration including the University of Arizona, the Brazilian Participation Group, Brookhaven

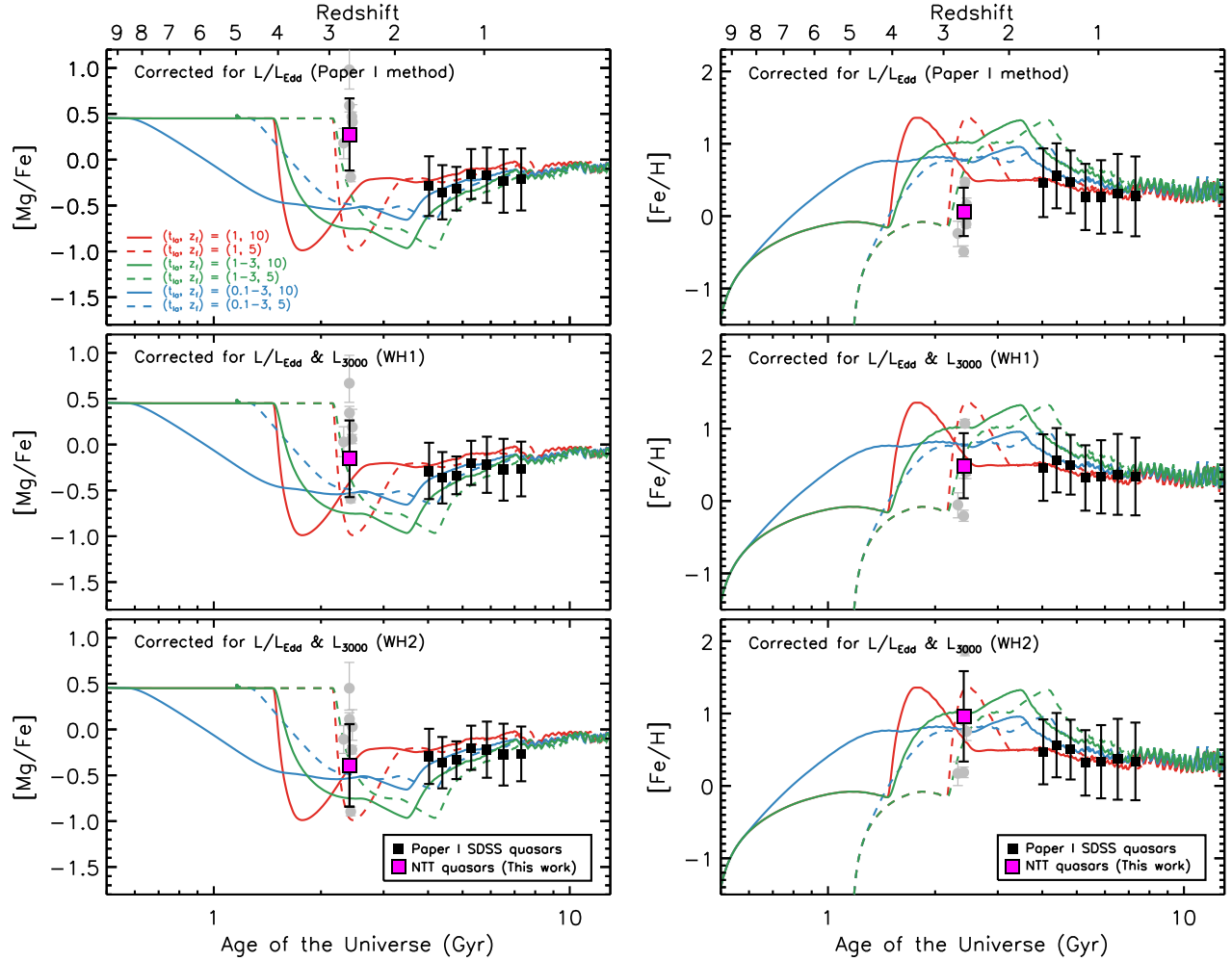


Figure 10. $[\text{Mg}/\text{Fe}]$ (left panels) and $[\text{Fe}/\text{H}]$ (right panels) as a function of the age of the universe. The abundances are derived from the measured EWs corrected for only L/L_{Edd} (top panels) and for both L/L_{Edd} and L with WH1 (middle panels) and WH2 (bottom panels). The overplotted curves are the chemical evolution models of quasar host galaxies for several prescriptions of the SNe Ia lifetime t_{Ia} in Gyr and the initial star formation redshift z_f (see Paper I).

National Laboratory, Carnegie Mellon University, University of Florida, the French Participation Group, the German Participation Group, Harvard University, the Instituto de Astrofísica de Canarias, the Michigan State/Notre Dame/JINA Participation Group, Johns Hopkins University, Lawrence Berkeley National Laboratory, Max Planck Institute for Astrophysics, Max

Planck Institute for Extraterrestrial Physics, New Mexico State University, New York University, Ohio State University, Pennsylvania State University, University of Portsmouth, Princeton University, the Spanish Participation Group, University of Tokyo, University of Utah, Vanderbilt University, University of Virginia, University of Washington, and Yale University.

REFERENCES

- Baldwin, J. A. 1977, *ApJ*, 214, 679
 Baldwin, J. A., Burke, W. L., Gaskell, C. M., & Wampler, E. J. 1978, *Nature*, 273, 431
 Barth, A. J., Martini, P., Nelson, C. H., & Ho, L. C. 2003, *ApJL*, 594, L95
 Boroson, T. A. 2002, *ApJ*, 565, 78
 Boroson, T. A., & Green, R. F. 1992, *ApJS*, 80, 109
 Boyle, B. J., Shanks, T., & Peterson, B. A. 1988, *MNRAS*, 235, 935
 Croom, S. M., Richards, G. T., Shanks, T., et al. 2009, *MNRAS*, 399, 1755
 Cutri, R. M., Skrutskie, M. F., van Dyk, S., et al. 2003, 2MASS All Sky Catalog of point sources.

- De Rosa, G., Decarli, R., Walter, F., et al. 2011, *ApJ*, 739, 56
- De Rosa, G., Venemans, B. P., Decarli, R., et al. 2014, *ApJ*, 790, 145
- Dietrich, M., Appenzeller, I., Vestergaard, M., & Wagner, S. J. 2002a, *ApJ*, 564, 581
- Dietrich, M., Hamann, F., Appenzeller, I., & Vestergaard, M. 2003, *ApJ*, 596, 817
- Dietrich, M., Hamann, F., Shields, J. C., et al. 2002b, *ApJ*, 581, 912
- Doi, M., Miyata, T., Yoshii, Y., et al. 2018, in *Society of Photo-Optical Instrumentation Engineers (SPIE) Conference Series*, Vol. 10700, Proc. SPIE, 107000W
- Dong, X.-B., Wang, J.-G., Ho, L. C., et al. 2011, *ApJ*, 736, 86
- Dong, X.-B., Wang, T.-G., Wang, J.-G., et al. 2009, *ApJL*, 703, L1
- Feltzing, S., Bensby, T., & Lundström, I. 2003, *A&A*, 397, L1
- Freudling, W., Corbin, M. R., & Korista, K. T. 2003, *ApJL*, 587, L67
- Grandi, S. A. 1982, *ApJ*, 255, 25
- Hamann, F., & Ferland, G. 1999, *ARA&A*, 37, 487
- Hamann, F., Korista, K. T., Ferland, G. J., Warner, C., & Baldwin, J. 2002, *ApJ*, 564, 592
- Ikeda, Y., Kobayashi, N., Kondo, S., et al. 2016, in *Proc. SPIE*, Vol. 9908, Ground-based and Airborne Instrumentation for Astronomy VI, 99085Z
- Iwamuro, F., Kimura, M., Eto, S., et al. 2004, *ApJ*, 614, 69
- Iwamuro, F., Motohara, K., Maihara, T., et al. 2002, *ApJ*, 565, 63
- Jiang, L., Fan, X., & Vestergaard, M. 2008, *ApJ*, 679, 962
- Jiang, L., Fan, X., Vestergaard, M., et al. 2007, *AJ*, 134, 1150
- Kausch, W., Noll, S., Smette, A., et al. 2015, *A&A*, 576, A78
- Kawara, K., Murayama, T., Taniguchi, Y., & Arimoto, N. 1996, *ApJL*, 470, L85
- Korista, K., Baldwin, J., & Ferland, G. 1998, *ApJ*, 507, 24
- Kurk, J. D., Walter, F., Fan, X., et al. 2007, *ApJ*, 669, 32
- Laor, A., Bahcall, J. N., Jannuzi, B. T., Schneider, D. P., & Green, R. F. 1995, *ApJS*, 99, 1
- Maiolino, R., Juarez, Y., Mujica, R., Nagar, N. M., & Oliva, E. 2003, *ApJL*, 596, L155
- Markwardt, C. B. 2009, in *Astronomical Society of the Pacific Conference Series*, Vol. 411, *Astronomical Data Analysis Software and Systems XVIII*, ed. D. A. Bohlender, D. Durand, & P. Dowler, 251
- Mazzucchelli, C., Bañados, E., Venemans, B. P., et al. 2017, *ApJ*, 849, 91
- McWilliam, A. 1997, *ARA&A*, 35, 503
- Mushotzky, R., & Ferland, G. J. 1984, *ApJ*, 278, 558
- Netzer, H. 1985, *MNRAS*, 216, 63
- Onoue, M., Bañados, E., Mazzucchelli, C., et al. 2020, *ApJ*, 898, 105
- Osmer, P. S., & Shields, J. C. 1999, in *Astronomical Society of the Pacific Conference Series*, Vol. 162, *Quasars and Cosmology*, ed. G. Ferland & J. Baldwin, 235
- Pâris, I., Petitjean, P., Ross, N. P., et al. 2017, *A&A*, 597, A79
- Peterson, B. M. 1997, *An Introduction to Active Galactic Nuclei* (New York Cambridge University Press)
- Pillepich, A., Nelson, D., Hernquist, L., et al. 2018, *MNRAS*, 475, 648
- Rayner, J. T., Cushing, M. C., & Vacca, W. D. 2009, *ApJS*, 185, 289
- Ross, N. P., McGreer, I. D., White, M., et al. 2013, *ApJ*, 773, 14
- Sameshima, H., Yoshii, Y., & Kawara, K. 2017, *ApJ*, 834, 203 (Paper I)
- Sameshima, H., Maza, J., Matsuoka, Y., et al. 2009, *MNRAS*, 395, 1087
- Schaye, J., Crain, R. A., Bower, R. G., et al. 2015, *MNRAS*, 446, 521
- Schneider, D. P., Richards, G. T., & Hall, P. B. 2010, *AJ*, 139, 2360
- Shang, Z., Wills, B. J., Robinson, E. L., et al. 2003, *ApJ*, 586, 52
- Shen, Y., Richards, G. T., Strauss, M. A., et al. 2011, *ApJS*, 194, 45
- Shields, J. C. 2007, in *Astronomical Society of the Pacific Conference Series*, Vol. 373, *The Central Engine of Active Galactic Nuclei*, ed. L. C. Ho & J. W. Wang, 355
- Shin, J., Nagao, T., Woo, J.-H., & Le, H. A. N. 2019, *ApJ*, 874, 22
- Smette, A., Sana, H., Noll, S., et al. 2015, *A&A*, 576, A77
- Sulentic, J. W., Zwitter, T., Marziani, P., & Dultzin-Hacyan, D. 2000, *ApJL*, 536, L5
- Thompson, K. L., Hill, G. J., & Elston, R. 1999, *ApJ*, 515, 487
- Tinsley, B. M. 1979, *ApJ*, 229, 1046
- Tolstoy, E., Hill, V., & Tosi, M. 2009, *ARA&A*, 47, 371
- Tsuzuki, Y., Kawara, K., Yoshii, Y., et al. 2006, *ApJ*, 650, 57
- Vestergaard, M., & Osmer, P. S. 2009, *ApJ*, 699, 800
- Vogelsberger, M., Zavala, J., Simpson, C., & Jenkins, A. 2014, *MNRAS*, 444, 3684
- Warner, C., Hamann, F., & Dietrich, M. 2003, *ApJ*, 596, 72
- . 2004, *ApJ*, 608, 136
- Wills, B. J., Netzer, H., & Wills, D. 1985, *ApJ*, 288, 94

Xu, Y., Bian, W.-H., Yuan, Q.-R., & Huang, K.-L. 2008,
MNRAS, 389, 1703

Yoshii, Y., Tsujimoto, T., & Kawara, K. 1998, ApJL, 507,
L113

Yoshii, Y., Tsujimoto, T., & Nomoto, K. 1996, ApJ, 462,
266

Yoshii, Y., Doi, M., Handa, T., et al. 2002, in 8th
Asian-Pacific Regional Meeting, Volume II, ed.
S. Ikeuchi, J. Hearnshaw, & T. Hanawa, 35–36

Yoshii, Y., Doi, M., Kohno, K., et al. 2014, in Society of
Photo-Optical Instrumentation Engineers (SPIE)
Conference Series, Vol. 9145, Proc. SPIE, 914507

Yoshii, Y., Doi, M., Kohno, K., et al. 2016, in Society of
Photo-Optical Instrumentation Engineers (SPIE)
Conference Series, Vol. 9906, Proc. SPIE, 99060R